



Quasi-static cyclic in-plane testing of masonry walls strengthened with a single-sided fabric-reinforced cementitious matrix overlay and flexible anchorage

Ö. S. Türkmen¹ · B. T. De Vries² · S. N. M. Wijte¹ · A. T. Vermeltoort¹

Received: 15 November 2018 / Accepted: 23 February 2019 / Published online: 22 March 2019
© The Author(s) 2019

Abstract

An experimental program was undertaken to assess the effectiveness of a new retrofit concept to improve the in-plane behavior of unreinforced clay brick walls by means of full-scale static-cyclic in-plane tests. The proposed seismic retrofit system combines two standalone retrofit measures for in-plane and out-of-plane strengthening of masonry walls. The in-plane reinforcement consists of a single-sided carbon Fabric-Reinforced Cementitious Matrix (FRCM) overlay, and anchors embedded with a flexible adhesive in the masonry. The out-of-plane reinforcement, which consisted of deep mounted Carbon Fibre Reinforced Polymer (CFRP) strips embedded with a flexible adhesive in the masonry, was included in the study to investigate the possible degrading effects of the deep groove on the in-plane behavior. A total of nine full-scale reinforced masonry walls with three different geometries were tested under three different axial loads. None of the specimens showed shear failure at both the reinforced and the as-built side. Cracking predominantly occurred at the interface between the bottommost bed-joint and the foundation beam. The out-of-plane reinforcement did not affect the in-plane strength, as no vertical shear cracks occurred. Moreover, it was found that the anchors increased both the rocking and sliding resistance of the walls. An analytical model was proposed covering the rocking and sliding resistance of the reinforced walls, providing a good approximation of the experimentally obtained in-plane strengths. Additional pull-out experiments showed that the testing scenario where the tensile forces in the anchor were transferred to CFRP strip, provided a good approximation of the analytically determined anchorage strength.

Keywords Shear · Seismic · Masonry · Retrofit · FRCM · Experiment

1 Background

In Groningen, an area in the Northeast of the Netherlands, earthquakes occur because of gas production from the Groningen field. Decades of gas production led to the depletion of the pressure of hydrocarbon gas within the reservoir pore space, causing the reservoir to compact. In turn, this compaction increases the mechanical loads acting on pre-existing geological faults within and close to the reservoir. Some small fraction of these faults become unstable and are therefore prone to slip. Abrupt slip on such a fault results in an earthquake that radiates seismic energy [1]. Although the magnitude of these induced earthquakes on Richter's scale is relatively low (< 3.5), they have a big impact on the buildings in the region due the soft surface soils in the area and the shallow depth (3 km beneath earth's surface) at which they occur [2]. As the majority of the buildings in Groningen are composed of cavity walls with single whyte

✉ Ö. S. Türkmen
o.s.turkmen@tue.nl

B. T. De Vries
bdevries@quakeshield.com

S. N. M. Wijte
s.n.m.wijte@tue.nl

A. T. Vermeltoort
a.t.vermeltoort@tue.nl

¹ Section Structural Design, Department of the Built Environment, Eindhoven University of Technology, P.O. Box 513, 5600 MB Eindhoven, The Netherlands

² QuakeShield (Joint Venture Royal Oosterhof Holman and SealteQ Group), P.O. Box 6, 9843 ZG Grijpskerk, The Netherlands

load bearing walls of unstrengthened clay brick masonry, and are designed to only resist wind loads, it is essential to improve the earthquake resistance of the existing buildings in the area to prevent collapse, with likely casualties. This definition of the problem in Groningen is identical to the first part of the introduction of the previous work of the authors [3]. The remaining part of the introduction contains duplicated (modified) passages from the previous work of Türkmen, De Vries, Wijte and Vermeltoort [3].

A broad range of strengthening techniques for enhancing the capacity of Unreinforced Masonry (URM) walls are available nowadays. Traditional strengthening methods such as reinforced concrete jacketing and steel frames, however, add considerable mass to the structure, are labor intensive, and generally alter the esthetics of a building [4]. A system of cement-based mortar matrix reinforced by continuous dry-fiber fabric is proposed for retrofitting masonry walls [5–8] and it is becoming more and more in use especially for in-plane strengthening. This strengthening system is known under different appellations: Fabric-Reinforced Cementitious Matrix (FRCM), Textile Reinforced Mortar (TRM), Textile-Reinforced Concrete (TRC) and Fiber Reinforced Cement (FRC) [9]. The FRCM strengthening technique is a sound alternative to FRP epoxy-bonded materials for reinforcing existing masonry elements for several reasons: (a) higher compatibility of the cement-based or lime-based mortar with the masonry supports than the epoxy adhesives, (b) higher adaptability to not perfectly plane surfaces (i.e. masonry textures with mortar joints or blocks with irregular shapes and dimensions, (c) low sensitivity to debonding phenomena [8]. Other advantages are breathability, fire resistance, reversibility, safety for the operators, better quality in terms of reversibility of the intervention in the case of historical and preserved buildings, and advantages in term of cost and time of installation [9–13].

Past experimental programs assessing innovative strengthening systems based on cementitious mortar matrices, highlighted a significant improvement in both in-plane and/or out-of-plane lateral strengths of masonry walls [6, 7, 10, 14–22]. Based on the response of medium-scale clay brick shear walls, beam-column type walls and beam type walls subjected to cyclic in-plane loading, Papanicolaou, Triantafillou, Karlos and Papathanasiou [10] concluded that FRCM overlays provide a substantial gain in strength and deformability. The authors reported that FRCM jacketing is much more effective than FRP. The increased effectiveness is about 15–30% in shear walls, 135% in beam-column type walls and 350% in beam type walls, on the basis of tests conducted [10]. With an experimental campaign medium-scale walls, Babaeidarabad, De Caso and Nanni [14] showed that the increase in ultimate in-plane strength is proportional to the amount of FRCM and ranged between 2.4 and 4.7 times that of the unstrengthened specimens.

The authors reported that toe-crushing failure occurred for wallettes with a calibrated reinforcement ratio higher than 4%, and therefore increments of FRCM beyond this value were claimed ineffective [14]. Ismail [15] investigated the in-plane behaviour of medium-scale clay brick shear walls strengthened with different types of FRCM systems. The shear strength of single-sided retrofitted wallettes ranged from 113 to 148%, whereas the shear strength of test wallettes with a double-sided FRCM retrofit ranged from 446 to 481% compared with the strength of the unstrengthened wallettes. The lower increase in shear strength for the single-sided retrofitted specimens was attributed to the unrestrained boundary conditions of the diagonal compression tests, as these specimens showed out-of-plane bending behaviour. This out-of-plane bending during the diagonal compression testing of single-sided FRCM retrofitted specimens, caused by the eccentric stiffness resulting from the application of the reinforcement on a single side, was also reported in other researches [16, 17]. Shabdin, Zargaran and Attari [16] tested medium-scale URM walls strengthened with FRCM under diagonal compression in order to consider the effect of strengthening system on the behavior of brick walls. The authors concluded that FRCM improved the diagonal load carrying capacity and deformation capacity, which caused the strengthened walls fail in a ductile manner. Marcarì, Basili and Vestroni [17] investigated the effectiveness of using a Basal TRM system for in-plane shear reinforcing of volcanic tuff stone masonry. The average increase in shear strength was approximately 40% for the single-side reinforced specimens, while the increase was 60% with double-side reinforced specimens. The authors also reported that the TRM system changed the failure mode of the panels from joint-sliding to diagonal cracking. Another experimental campaign carried out on medium-scale tuff-masonry walls also showed that strengthened walls did not fail for the characteristic diagonal sliding fracture, generally developing in unreinforced masonry walls at the mortar-to-brick interface [18]. The ultimate load in diagonal compression (and the corresponding shear strength) for strengthened walls were reported to be between four and six times greater than the one observed for bare walls [18]. Ismail and Ingham [19] conducted an experimental program with full scale reversed cyclic in-plane testing of FRCM strengthened URM walls. The authors observed the strength increment due to TRM strengthening to range from 128% to 136% when the URM test walls were loaded in-plane, with a notable increment in deformation capacity and ductility.

For the out-of-plane strengthening of masonry walls the FRCM system requires application to both faces of a wall. In case of strengthening of load bearing leafs of cavity walls, this would require the temporary rehousing of the occupants in order to install the FRCM layer from within the building, as well as the removal of the

façade of the building for the installation of the FRCM layer on the cavity facing side of the load bearing wall. Cost effective retrofitting can be enhanced by installing deep mounted CFRP out-of-plane reinforcement, where FRP strips or rods are inserted into deep vertical grooves cut in the surface of a wall. The CFRP strips offer additional out-of-plane flexural strength to the wall for both out-of-plane loading directions whilst only installing the reinforcement from one side of the wall, leading to cost-effective retrofitting [23, 24]. This system uses a viscous-elastic epoxy instead of a conventional stiff epoxy for the installation of the FRP strips, because the implementation of a conventional stiff adhesive for deep mounting the CFRP strips results in premature splitting failure in the masonry [25]. Next to making deep mounting possible, using a viscous-elastic epoxy (Young's modulus $< 50 \text{ N/mm}^2$) instead a conventional stiff adhesive (Young's modulus $\sim 10,000 \text{ N/mm}^2$), a significant increase in terms of ductility and maximum withstandable load is reached and critical crack development is prevented [23, 24, 26]. Similar findings were previously reported by Kwiecień [27] and Derkowski, Kwiecień and Zajac [28].

A schematic overview of the proposed combined reinforcement concept is shown in Fig. 1. While the influence of FRCM reinforcement on the in-plane behaviour of masonry wall panels has been a popular subject of research for the past years, the influence of the aforementioned combination of retrofit measures on the in-plane shear capacity of masonry has not been investigated before. Moreover, this experimental program aims to investigate the possible degrading effect of the proposed out-of-plane strengthening system on the in-plane shear strength of masonry panels. The aim of the experimental campaign for this study was to determine the effectiveness of a one-sided FRCM reinforcement combined with DM CFRP strips to improve the in-plane shear

resistance of clay brick masonry walls. In this experimental campaign, static-cyclic in-plane shear tests were performed (cantilever configuration) on full-scaled masonry walls strengthened with this combined reinforcement system. Additional pull-out experiments were conducted to gain more insight on the behavior of foundation anchors, embedded in the same flexible adhesive as the CFRP strips. Finally, the experimental results were compared to the outcomes of existing design codes, to check the validity of these models for this combined retrofit system.

2 Experimental program

2.1 Materials and characterization

This materials and characterization section is mostly identical to §2.1 of the previous work of the authors [3]. The clay bricks used in this research had dimensions of $205 (\pm 4) \times 95 (\pm 2) \times 50 (\pm 2) \text{ mm}^3 (l_b \times w_b \times h_b)$. Several mechanical characteristics of the used clay bricks were determined with an experimental program conform the corresponding standards. The bricks had a mean compressive strength f_c of 31.7 N/mm^2 ($n = 12$; $\text{COV} = 7.4\%$), where n is the amount of tested specimens respectively. The compressive strength of the clay bricks were determined following the EN 772-1 [29] standard using gypsum capping and half bricks. The mean splitting tensile strength f_{st} (determined conform ASTM C1006-07 [30]) and flexural tensile strength f_t (obtained following ASTM C67-03 [31]) of the bricks were found to be 3.34 N/mm^2 ($n = 12$; $\text{COV} = 8.7\%$) and 5.89 N/mm^2 ($n = 9$; $\text{COV} = 7.4\%$). The mean flexural tensile strength of the mortar specimens was found to be 3.6 N/mm^2 ($n = 8$, $\text{COV} = 16.5\%$), and the mean compressive strength of the mortar was 10.6 N/mm^2 ($n = 16$; $\text{COV} = 20.7\%$). Both the

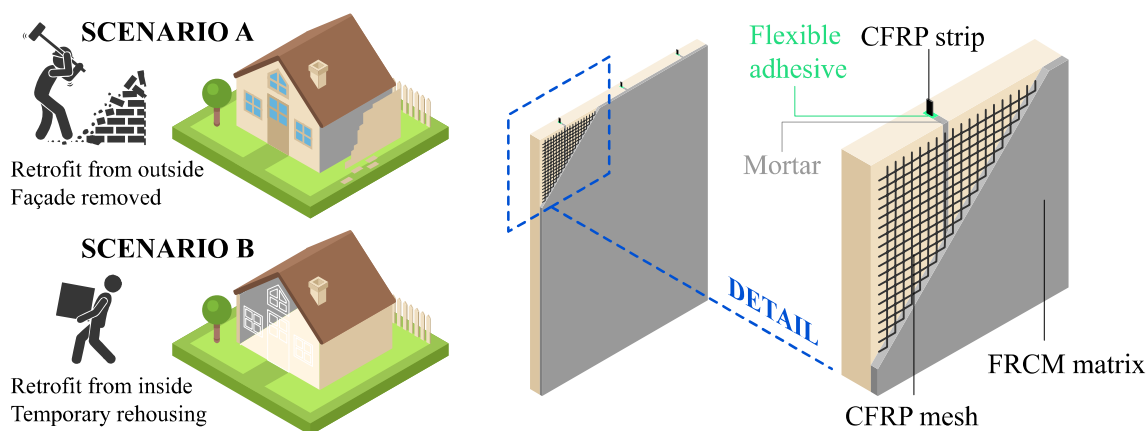


Fig. 1 Reinforcement concept for a house with cavity walls, where the FRCM reinforcement and deep mounted CFRP strips are installed from either the inside (temporary rehousing occupants) or the outside

(removal of the façade) on the load bearing walls to secure cost-effective retrofitting [3]

flexural tensile strength and the compressive strength of the mortar specimens were determined according to EN 1015-11 [32]. Compression tests were performed on three masonry specimens, consisting of 6 brick high masonry prisms, under displacement control with a loading speed of 0.20 mm/min. The average compressive strength (f_m) of the specimens was 14.8 N/mm² (COV = 6.1%). The Young’s modulus was determined as a secant modulus at 35% of the compressive strength in accordance with EN 1052-1 [33]. The average Young’s modulus (E) of the masonry prisms was found to be 3100 N/mm² (COV = 2.5%).

In order to determine the mechanical properties of the masonry under shear in accordance with EN 1052-3 [34], a total of 9 triplet shear tests was performed at three different normal stress levels: 0.2, 0.6 and 1.0 N/mm². For each specimen the relation between the applied normal stress and the shear strength has been established. The ratio between the compressive stress and the shear strength of the masonry was obtained using a linear regression. The parameters for the Coulomb’s friction criterion follow from Eq. (1):

$$f_v = f_{v,0} + \mu_{ma} \sigma_n \tag{1}$$

with $f_{v,0}$, μ_{ma} and σ_n being the initial shear strength, friction coefficient and axial load respectively. The residual shear strength ($f_{v,0,res}$) and residual coefficient of friction ($\mu_{ma,res}$) were determined by applying the same linear regression analysis when a plateau was reached in the post-peak phase. The mechanical properties of the materials used for building the specimens for this study are summarized in Table 1. The obtained values regarding the mechanical properties of masonry under shear correspond well with the results of the study carried out by Jafari, Rots, Esposito and Messali [35] on the material properties characterization of Dutch URM, and the values proposed in the Dutch Practical Guideline for the seismic assessment of local buildings in Groningen, NPR9998 [36].

The reinforced mortar used for the mortar matrix of the FRCM overlay was a polymer modified mortar based on organic binders, polymer fibres and selected aggregates, with a maximum grain size of 1.8 mm. The dry mortar and polymer fibres are shown in Fig. 2a. The additional reactive components, which were mixed into the reinforcement mortar, bonded with the amorphous silica on the CFRP mesh. This ensured an improved adhesion between the mesh and

the cementitious matrix. For the preparation of the reinforced mortar, a plastic bonding agent was used in order to improve the adhesion of the cementitious matrix to the clay brick substrate. This was done by mixing 110 g of the plastic bonding agent per 10 kg of prepared mortar. The reinforced mortar was prepared following the manufacturer’s instructions by adding 2.6 L of water to a bag of 25 kg dry mortar. Both the flexural tensile strength and the compressive strength of the reinforced mortar specimens were determined according to EN 1015-11 [32]. The average flexural tensile strength of the reinforced mortar specimens was found to be 7.58 N/mm² ($n=9$; COV = 11.7%). The mean compressive strength of the reinforced mortar was 62.6 N/mm² ($n=12$; COV = 1.6%). The weight density was 2138 kg/m³ ($n=6$; COV = 1.7%).

The bidirectional CFRP mesh, with a fibre weight density of 1.79 g/cm³ and about 3 mm width per thread, had a square aperture dimension of approximately 50 × 50 mm². The theoretical cross section of the carbon fibre for design was 44 mm². The Young’s modulus, tensile strength and elongation at rupture of the mesh as provided by the supplier are > 240 kN/mm², > 4300 N/mm² and 1.75% respectively for the carbon FRP mesh. The prefabricated (pultruded) CFRP strips were 20 mm in width and 1.4 mm in thickness and have a fibre volume content of > 68%. The Young’s modulus, tensile strength and elongation at rupture of the CFRP strip was found to be 215 kN/mm², 2876 N/mm² and 1.59% respectively.

The material properties for the two-component viscous-elastic adhesive were obtained following ISO 527-1 [37] using three specimens at a loading rate of 10 mm/min. The Young’s modulus was determined as the secant modulus between 0.5% and 5% of the tensile strength, and was found to be 16.0 N/mm² (COV = 1.7%). The tensile strength and elongation of rupture were determined as 4.3 N/mm² (COV = 0.9%) and 72.1% (COV = 3.5%).

Tensile tests were performed using a clevis-type gripping mechanism following the American guideline AC434.13 [34] with a metal tab contact length of 150 mm as recommended by Donnini and Corinaldesi [13]. The uncracked FRCM slab had a tensile strength (σ_m) of 4.31 N/mm² ($n=9$; COV = 14.9%), a corresponding strain (ϵ_m) of 0.016% ($n=8$; COV = 13.5%) and a Young’s modulus of 27,680 N/mm²

Table 1 Mechanical properties of the masonry materials used for building the specimens

	ρ (kg/m ³)	E (N/mm ²)	f_t (N/mm ²)	f_{st} (N/mm ²)	f_c (N/mm ²)	$f_{v,0}$ (N/mm ²)	μ_{ma} (-)	$f_{v,0,res}$ (N/mm ²)	$\mu_{ma,res}$ (-)
Clay brick	1738 ^d	–	5.89 ^{a, e, m}	3.34 ^{f, n}	31.7 ^{g, o}	–	–	–	–
Building mortar	1745 ^h	–	3.6 ^{a, i, m}	–	10.6 ^{j, p}	–	–	–	–
Masonry	–	3100 ^{k, q}	–	–	14.8 ^{l, q}	0.38 ^{b, r}	0.75 ^{b, r}	0.02 ^{c, r}	0.81 ^{c, r}

^aFlexural, ^bObtained from a linear regression with $R^2=0.77$, ^cObtained from a linear regression with $R^2=0.96$, ^d $n=12$; COV = 3.6% ^e $n=9$; COV = 7.4%, ^f $n=12$; COV = 8.7%, ^g $n=12$; COV = 7.4%, ^h $n=8$; COV = 1.9%, ⁱ $n=8$; COV = 16.5%, ^j $n=16$; COV = 20.7%, ^k $n=3$; COV = 6.1%, ^l $n=3$; COV = 2.5%, ^mASTM C67-03 [31], ⁿASTM C1006-07 [30], ^oEN 772-1 [29], ^pEN 1015-11 [32], ^qEN 1052-1 [33], ^rEN 1052-3 [34]

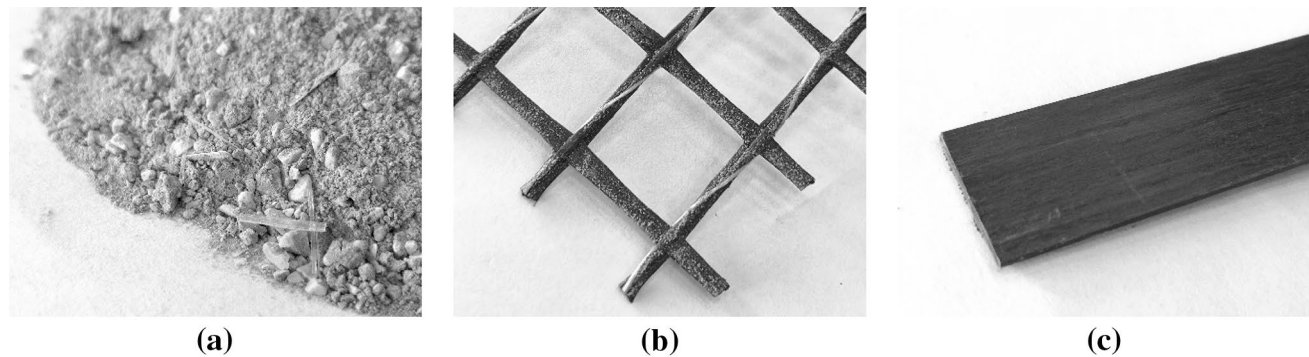


Fig. 2 Photo of the materials used for reinforcement: close-up of the dry reinforced mortar, showing the polymer fibres (a), CFRP mesh with the amorphous silica intended for improved adhesion (b) and CFRP strip (c)

($n = 8$; $COV = 6.9\%$). The stresses for the uncracked case were calculated with respect to the cross-sectional area of the reinforced mortar. For the cracked FRCM slab, the stresses were calculated with respect to the cross-sectional area of the CFRP mesh (Table 2). The ultimate stress in the mesh, σ_{ult} , was found to be of 1628 N/mm^2 ($n = 9$; $COV = 10.2\%$), with a corresponding ultimate strain (ϵ_{ult}) of 1.91% ($n = 6$; $COV = 14.9\%$). The Young's modulus of the cracked specimen, calculated as the slope of the segment of the stress–strain diagram between $0.90 \sigma_{ult}$ and $0.60 \sigma_{ult}$ (following AC434.13 [38]), was $70,920 \text{ N/mm}^2$ ($n = 6$; $COV = 15.3\%$). The main failure mode observed was slippage of the CFRP mesh within the mortar matrix. The mechanical properties of the materials used for reinforcing the specimens are summarized in Table 3.

2.2 Building the in-plane test specimens

The wall specimens for the static-cyclic in-plane shear tests were built in the testing laboratory of QuakeShield in Grijpskerk, the Netherlands. The specimens were built on a reinforced concrete foundation beam by an experienced mason. The masonry walls were nominally 2450 mm high (h_w) and had a thickness (t_w) of 100 mm . The lengths of the specimens (l_w) were 1100 mm (for the S specimens), 2000 mm (for the M specimens) and 4000 mm (for the L specimens). For each configuration three specimens were built in order to test the effect of axial load q_v on the in-plane behavior for each geometry. The axial loads were 0.15 , 0.3 or 0.5 N/mm^2 , with the only exception being specimen S1 (0.20 N/mm^2), due to control difficulties of low axial forces. An overview of the test specimens is provided in Table 3.

The concrete foundation beam had a height (h_c) of 180 mm and a width (t_c) of 180 mm . It should be noted that the reinforced concrete beam used for the M-specimens was 60 mm shorter than the length of these wall specimens. These wall specimens therefore extended 30 mm over the foundation beam at both ends. The mortar for the masonry

specimens was prepared in the laboratory and the walls were built in running bond. Both the bed and head joints had a nominal thickness of 12 mm and were fully filled. All walls cured in air in the unheated laboratory ($0\text{--}10 \text{ }^\circ\text{C}$) for at least 28 days before strengthening.

2.3 Reinforcing the in-plane test specimens

Figure 3 presents photographs of the installment of the reinforcement system in a practical application (anchorage not included). The reinforcement process however is uniform. Schematic overviews of the reinforced S-, M- and L- specimens are provided in Fig. 4. Details and geometric properties are provided in Fig. 5 and Table 4. After the walls were sufficiently cured (± 28 days) the strengthening process started by milling a number (n_g) of vertical grooves ($n_g = 2$, $n_g = 3$ and $n_g = 5$ for S, M and L specimens respectively) of 65 mm depth (d_f) and 10 mm width (b_f), spaced 850 mm (l_{strip}) apart. The distance of the outer grooves to the edges (l_{edge}) was 150 mm for the S and M specimens and 300 mm for the L specimens. The dust in the groove was removed with compressed air. The CFRP strips with a cross-section of $20 \times 1.4 \text{ mm}^2$ ($b_p \times t_p$) were cleaned with acetone after cutting the strips into the specified length. A layer of primer was then applied to the groove to obtain an improved bond of the adhesives to the masonry. Afterwards, the CFRP strips were inserted into the groove that was partially filled with the flexible adhesive. The vertical grooves at the side ends were widened to 25 mm (b_f') till a depth of 35 mm (d_f') and a height of 500 mm . In each specimen two 12 mm (D_s) ribbed reinforcement bars (B500B) with a length of 650 mm (l_a) were fixed with a conventional stiff adhesive (HIT-HY 100) inside a borehole of 150 mm in depth ($l_{a,stiff}$) and angle of 30° degrees in the foundation beam. The remaining part of the steel rods were embedded in the visco-elastic adhesive within the aforementioned widened grooves over a length of 500 mm ($l_{a,flexible}$). Excess adhesive till a depth of 30 mm

Table 2 Mechanical properties of the materials used for reinforcing the specimens

	ρ (kg/m ³)	E (N/mm ²)	f_t (N/mm ²)	σ_m (N/mm ²)	ϵ_m (%)	σ_{ult} (N/mm ²)	ϵ_{ult} (%)	f_c (N/mm ²)
Flexible adhesive	–	16.0 ^{d, r}	4.3 ^{e, r}	–	–	–	–	–
CFRP strip	1700	215,000 ^{f, r}	2876 ^{g, r}	–	–	–	1.59 ^{h, r}	–
CFRP mesh	1790	≥ 240	≥ 4300	–	–	–	≥ 1.7	–
Mortar matrix	2138 ⁱ	≥ 25,000	7.58 ^{a, j, s}	–	–	–	–	62.55 ^{k, s}
FRCM uncracked ^b	–	27,680 ^l	–	4.31 ^m	0.016 ⁿ	–	–	–
FRCM cracked ^c	–	70,920 ^{o, t}	–	–	–	1628 ^{p, t}	1.91 ^{q, t}	–

^aFlexural, ^bStresses calculated with respect to the cross-sectional area of the reinforced mortar, ^cStresses calculated with respect to the cross-sectional area of the CFRP mesh, ^d $n=3$; COV = 1.7%, ^e $n=3$; COV = 0.9%, ^f $n=5$; COV = 1.0%, ^g $n=5$; COV = 3.4%, ^h $n=5$; COV = 14.7%, ⁱ $n=6$; COV = 1.7%, ^j $n=9$; COV = 11.7%, ^k $n=12$; COV = 1.6%, ^l $n=8$; COV = 6.9%, ^m $n=9$; COV = 14.9%, ⁿ $n=8$; COV = 13.5%, ^o $n=6$; COV = 15.3%, ^p $n=9$; COV = 10.2%, ^q $n=6$; COV = 19.4%, ^rISO 527-1 [37], ^sEN 1015-11 [32], ^tAC434.13 [38]

Table 3 Overview of the geometry of the specimens and the applied axial loads

	Unit	S			M			L		
l_w	mm	1100			2000			4000		
h_w	mm	2450			2450			2450		
t_w	mm	100			100			100		
		S1	S2	S3	M1	M2	M3	L1	L2	L3
q_v	N/mm ²	0.2	0.3	0.5	0.15	0.3	0.5	0.15	0.3	0.5

(d_{ff}) in the standard grooves and 10 mm (d_{ff}') in the widened grooves was removed using a scraper.

After the placement of the strips and anchors, the walls were left to cure for one day before applying the single-sided FRCM overlay. The masonry surface was wetted prior to the mortar matrix application to secure proper adhesion. A thin layer of mortar was subsequently applied to the masonry surface by hand. The remaining parts of the grooves were also filled with the same mortar. The CFRP mesh was then applied on the mortar matrix surface and was pressed into the mortar matrix. After placing the CFRP mesh in the mortar a new thin layer of mortar was applied to embed the CFRP mesh, resulting in a nominal FRCM layer thickness of 15 mm (t_{FRCM}). The specimens were left to cure in the laboratory environment for a minimum of 28 days before starting the experimental program.

2.4 In-plane test setup

The static-cyclic in-plane shear tests were performed in the test setup of QuakeShield. The test setup is illustrated in Fig. 6, and shown in picture in Fig. 7. The frame of the test setup is formed by two post-aligned steel frames which were interconnected. The basis of the frame is a rectangular closed portal frame (A in Fig. 4) in which the specimen was placed. The bottom beam of it passes through the portal frame and supported the steel shore (C) that connects to the portal frame at the position of the horizontal actuator. Steel beam B in Fig. 4 takes care of the stability of the test

setup in transverse direction. All steel profiles of the test frame are interconnected by weld connections thus minimizing movement in the connections. The test specimens were supported at the bottom side by a foundation formed by a reinforced concrete beam. This foundation beam was connected to a 15 mm steel plate with a fast-curing epoxy. The steel plate allowed for a connection between the specimen and the test setup. Besides the epoxy-connection with the bottom steel plate, the foundation beam was also kept in place by a mechanical connection (steel brackets) that covered the topside of the beam.

At the topside the specimens were provided with a steel plate which enabled a connection between the specimens and the loading beam. In order to ensure a uniform distribution of the vertical load, rubber pads were placed between the loading beam and the steel plate which connected the specimens to the test setup. This steel plate was in turn provided with 40 mm thick steel blocks which were positioned such that they fitted exactly between the rubber pads. These steel blocks were used to transfer the horizontal load from the loading beam to the specimen (Fig. 6). The steel plates were attached to the specimens with a fast-curing adhesive after lowering the loading beam. After a minimum curing time of 24 h, the experiment was started.

The horizontal load was generated by a horizontally positioned hydraulic actuator with a capacity of 500 kN. The horizontal load was applied in both West direction (also referred to as push direction) and East direction (also referred to as pull direction). A loading beam distributed this horizontal

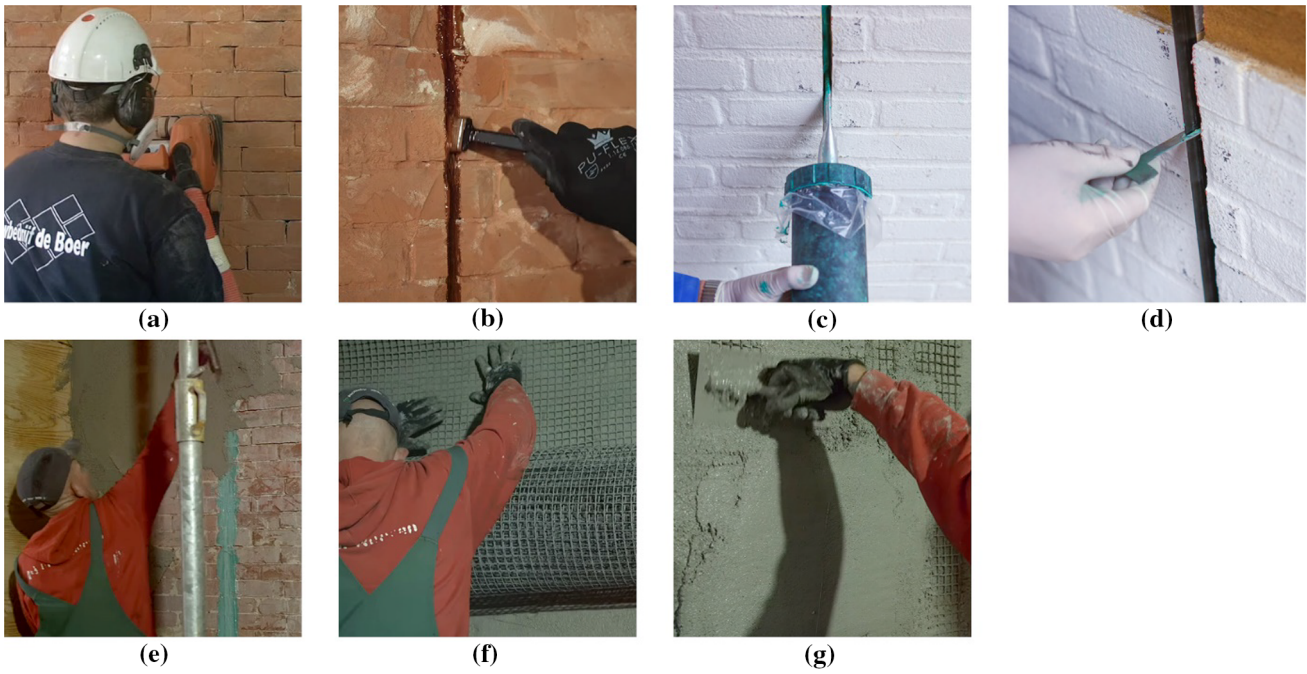


Fig. 3 Photos showing the different stages of the reinforcement process, taken at a retrofitted building by QuakeShield: milling the grooves (a), cleaning the grooves with acetone (b), injecting flexible adhesive in the groove (c), pushing the CFRP strip into position with

a positioning fork (d), installing the first layer of FRCM matrix (e), pressing the CFRP mesh into the FRCM matrix (f), application of second layer of FRCM matrix (g)

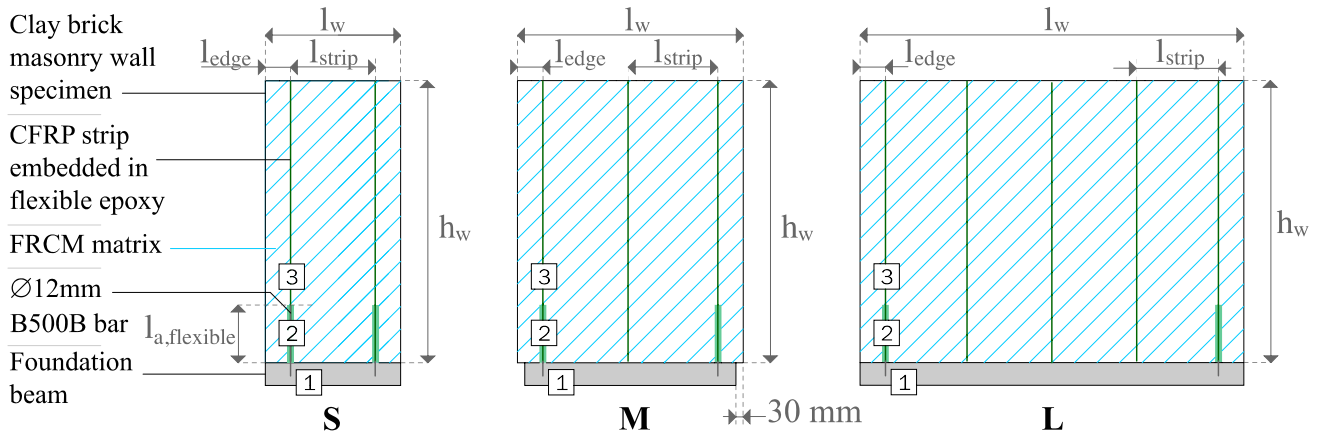


Fig. 4 Schematic overview of the reinforced S, M, and L specimens

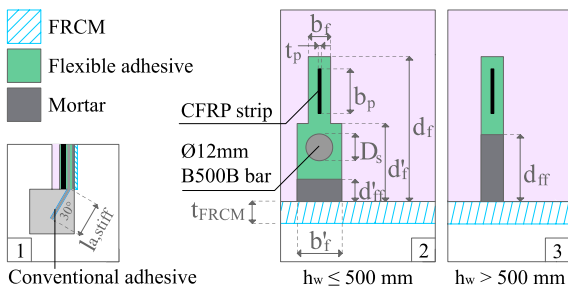


Fig. 5 Detail of the reinforced specimens

load over the topside of the specimen. For the sake of symmetry in the push and pull cycles the force exerted by the horizontal actuator engaged in the center of the load beam using two steel arms. The load beam was stiffened at the top with an IPE-profile on which two vertically positioned hydraulic actuators with a capacity of 200 kN each, provided the desired vertical load on the test specimen. At the topside the vertical jacks were fixed in position against the frame of the test setup. Because the load beam would translate horizontally throughout the test the vertical jacks were connected

Table 4 Geometrical properties of the reinforced specimens

Description	Symbol	Value
Distance between outer CFRP strips and the edge of the walls	l_{edge}	150/300 ^a
Distance between the CFRP strips	l_{strip}	850
Embedded length ribbed reinforcement bars in flexible adhesive (in the wall)	$l_{a,flexible}$	500
Embedded length ribbed reinforcement bars in stiff adhesive (in the foundation)	$l_{a,stiff}$	150
Thickness of the CFRP strip	t_p	1.4
Width of the CFRP strip	b_p	20
Diameter of the ribbed reinforcement bars	D_s	12
Width of vertical groove	b_f	10
Depth of the vertical groove	d_f	65
Width of widened vertical groove	b'_f	25
Depth of the widened vertical groove	d'_f	35
Depth of the groove filled with mortar matrix	d_{ff}	30
Depth of the widened groove filled with mortar matrix	d'_{ff}	10
Nominal thickness of the FRCM layer	t_{FRCM}	15

All presented values are in mm

^a150 for S and M specimens; 300 for L specimens

to the beam by means of crane trolleys. The crane trolleys were in turn connected to the hydraulic actuator by a load pin, which also enabled rotation of the crane trolley. This load pin also monitored measured the load exerted by the actuators. Both load pins were calibrated to a maximum force of 120 kN and had an accuracy of 0.3%. The horizontal load which was exerted by the horizontal actuator was monitored by a load cell positioned at each of the two steel arms which connects the actuator to the center of the loading beam. In addition to these load measurement devices the horizontal and vertical loads were checked by measuring the oil pressure within the hoses of the hydraulic power pack.

Displacement and deformation measurements were conducted by laser sensors with an accuracy of 7 microns. Laser

sensor 12 in Fig. 6 was used for controlling the test and for constructing the force-displacement plots. This sensor was connected to the steel plate on top of the specimens and displacements were measured relative to a detached frame. Vertical deformation measurements were conducted on the small specimens. These deformations were measured by means of two laser sensors which were applied on telescopic tubes (8 and 9). The telescopic tubes covered nearly the complete height of the specimens and monitored the vertical deformation of the specimen. Shear deformations were measured on the medium and large specimens by laser sensors on diagonally positioned telescopic tubes (6 and 7). Slip of the wall specimens over the bottommost bed joint was measured by a laser sensor positioned on a

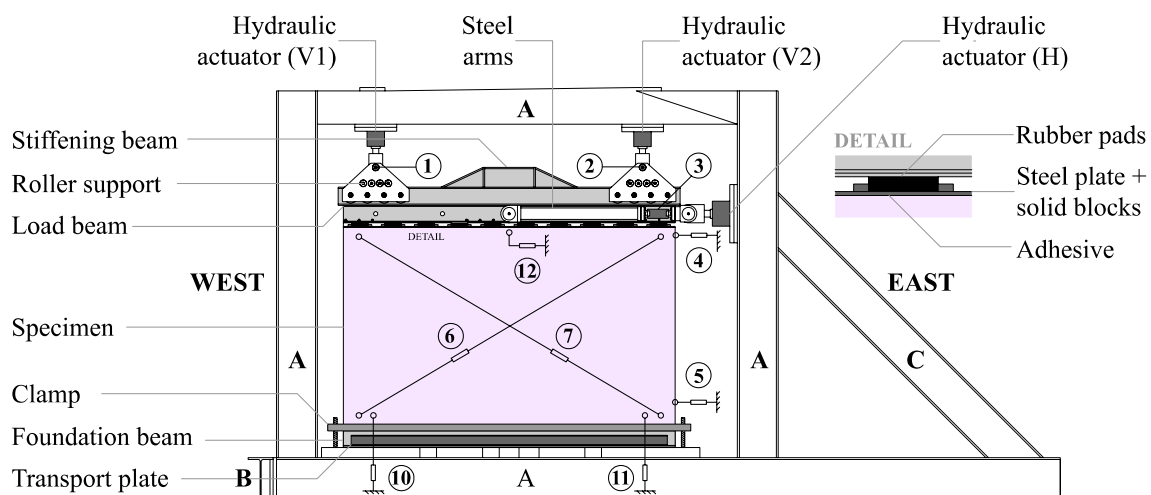


Fig. 6 Schematic overview of the shear test setup. West direction = push; East direction = pull

Fig. 7 Photo of the shear test setup



detached measurement frame (5). The same frame was used for the positioning of a laser sensor which measured the displacement of the East top of the specimen (4). Possible vertical uplift at the position of the steel anchors was measured by two laser sensors placed on detached measurement frames (10 and 11). All measuring devices were connected to a PLC-system which processed the data in real time. This data was then forwarded by the PLC-system to a laptop and monitored by the researcher. During the tests the nature and extent of the cracking pattern was continuously observed and noted.

The cantilever configuration was chosen for this testing program, where vertical deformation and rotation of the loading beam is not restrained (i.e. free rotation at the top). The vertical force of both actuators was kept constant during the complete course of the tests. The vertical loads exerted by both actuators was therefore not depending on the exerted horizontal load nor the horizontal displacement. After applying the vertical pre-compression load the wall specimens were subjected to cyclic shear loading. The cyclic shear load was applied using computer controlled displacement steps, starting from 0.26 mm with a speed of 0.2 mm/s. Each displacement step was applied two times in both loading direction forming one load cycle, before increasing the target displacement with 40%, based on the FEMA [39] protocol. This continued until a target displacement of ± 40 mm, which was the maximum stroke of the horizontally oriented hydraulic actuator.

2.5 Direct pull-out tests

The force in the anchors, especially during the rocking behavior of a reinforced specimen, is a relevant parameter

for modelling purposes. With the test setup presented in the previous paragraph and the limitations in the lab, the measurement of the force in the anchors was difficult to realize. In order to gain more understanding on the mechanical behavior of the flexible anchor connection, additional small-scale direct pull-out tests were performed. Two possible scenarios were considered as shown in Fig. 8, regarding the transfer of the tensile forces in the anchor into the reinforced specimen,

- Scenario A: The tensile forces in the anchor are fully transferred to the masonry substrate via the adhesive.
- Scenario B: The tensile forces in the anchor are fully transferred to the CFRP strip, via (predominantly) the adhesive and the masonry substrate.

For both configurations 3 specimens were built of 8 (Scenario A) and 12 (scenario B) bricks in height, coded DPT-A and DPT-B respectively. The installation and positioning of the anchor and strip was conducted according to the same reinforcement method as described in Sect. 2.3. Only anchors were installed on the DPT-A specimens. The anchors installed in the DPT-B specimen, were bonded to the bottom 490 mm of the specimen. This was done to maintain a consistent anchorage length with the anchors of the DPT-A specimens. The installed CFRP strip on the DPT-B specimen, were bonded over the entire specimen length of 740 mm. The specimens are illustrated in Fig. 9. In experimental conditions, scenario A was realized by restraining the masonry prism using a steel plate. Scenario B was realized by clamping the extended piece of the CFRP strip, rather than using a steel plate. An overview of the direct pull-out test setup is provided in Fig. 10.

The direct pull-out tests were conducted on a 250 kN Instron universal testing machine (Fig. 11). For the DPT-A specimens (Fig. 11a), the installation process started by carefully positioning the prism under the loading grips of the testing equipment, with the specimen resting on two support blocks. Hard cardboard was put on the top of the prism to prevent stress concentrations due to a possible non-flat surface of the brick. Afterwards the steel restraint plate at the loaded end was placed on top of the prism. To prevent undesirable wedge type failure modes when using partial end restraint, a full restraint in the form of a 25 mm thick solid steel plate with three openings was selected. The centrally located opening allowed the loaded end of the ribbed steel anchor to pass through. The smaller two openings allowed the LVDT (linear variable differential transformer) sensors to rest on the specimen. The specimen was then lifted up, which made it possible for the prism to find its own balance point and thus minimize the eccentricity caused by imperfect installation of the anchor. Using M12 threaded steel rods, the steel restraint plate was bolted tightly to the base of the setup. Four LVDT's were installed prior to the load application process. The upper two LVDT's (1 and 2) measured the loaded end slip, whereas the bottom two LVDT's (3 and 4) measured the free end slip.

The installation process of the DPT-B specimens (Fig. 11b) was slightly different from the DPT-A specimens. Aluminium plates of 100 mm in length, 20 mm in width and 2 mm in thickness were used to tab the CFRP strips. After the tabs were roughened with sandpaper and thoroughly cleaned with acetone, the tabs were glued to both sides of the extending CFRP strip using high strength and fast curing 2-component epoxy adhesive. The prism was positioned under the loading grips of the testing equipment, with the specimen resting on two support blocks. The specimen was then lifted up via the aluminium grip plates. The extending anchor was clamped using the grips at the base of the installation. Prior to the load application process, four LVDT sensors were installed. The upper two LVDT's (1 and 2) measured the loaded end slip of the CFRP strip, whereas the bottom two LVDT's (3 and 4) measured the loaded end slip of the steel anchor. The mean of two LVDT's was used to establish the corresponding slip. The pre-tension load was 1.0 kN for all specimens. After resetting the sensors, the experiment was started with a pull-out speed of 0.5 mm/min on the loading grips.

3 Test results

This chapter will provide an overview of the obtained results during the experimental campaign. The first five paragraphs focus on the in-plane shear experiments, covering overall results, failure modes, strength and drift values, wall response parameters and finally the uplift of the anchors. The final paragraph covers the direct pull-out experiments of both load transfer scenarios.

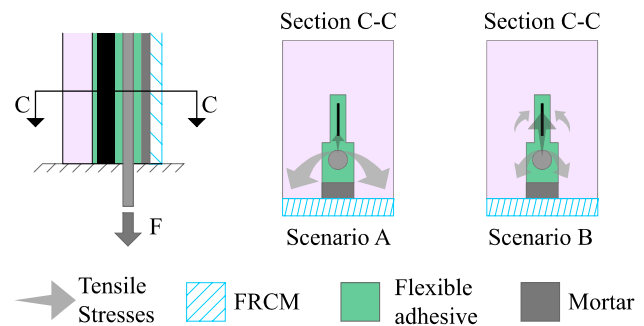


Fig. 8 Possible stress transfer scenario's from the anchor to the masonry/CFRP strip

3.1 Overview in-plane shear test results

A summary of the obtained in-plane test results is given in Table 5. The maximum forces in both the pull ($H_{max,east}$) and push cycles ($H_{max,west}$) is reported. Moreover the maximum displacement δ_{max} , the maximum drift Δ_{max} [calculated in accordance with Eq. (2)] and the failure modes are shown. These parameters are discussed in the following paragraphs.

$$\Delta_{max} = \delta_{max}/h_w \quad (2)$$

3.2 Failure modes in-plane shear tests

The failure modes of all specimens are illustrated in Fig. 12. None of the specimens showed any shear damage at the treated or untreated surfaces. As failure only occurred at the bottom side of the specimens, the upper part of the walls is not shown in the illustrations in Fig. 12. All tested specimens showed initial cracking at the bottom corners. These initial cracks propagated over the complete length of the specimen during subsequent loading cycles. Cracking mainly occurred at the interface between the bottommost bed-joint and the concrete foundation beam. The expected formation of cracks due to the vertical shear stress concentrations caused by the deep grooves (needed for the out-of-plane reinforcement) did not occur.

All specimens started to show rocking behaviour during the tests. For specimens S3, M1, M2, M3 rocking of the specimen was followed by crushing of the specimens' bottom corners. The uplift of the specimen had the effect of reducing the compressive zone which eventually led to toe-crushing. Due to the relatively low compression forces acting on specimen S1 and S2 these specimens did not show compressive failure.

For specimen S1, first cracking was observed at a horizontal force of about 8 kN in push direction. During the pull cycles not only similar cracking of the bed joint took place but also partial detachment of the concrete foundation beam from the steel plate occurred. Consequently some uplift of the West side of the foundation beam was observed due to

Fig. 9 Specimens for the direct pull-out tests

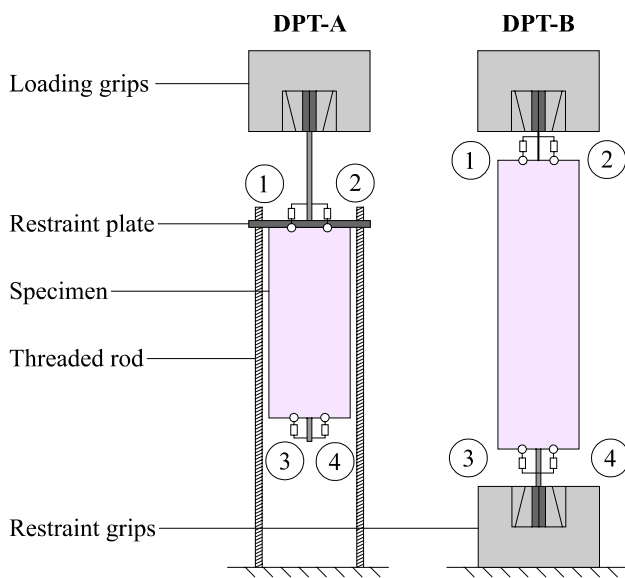
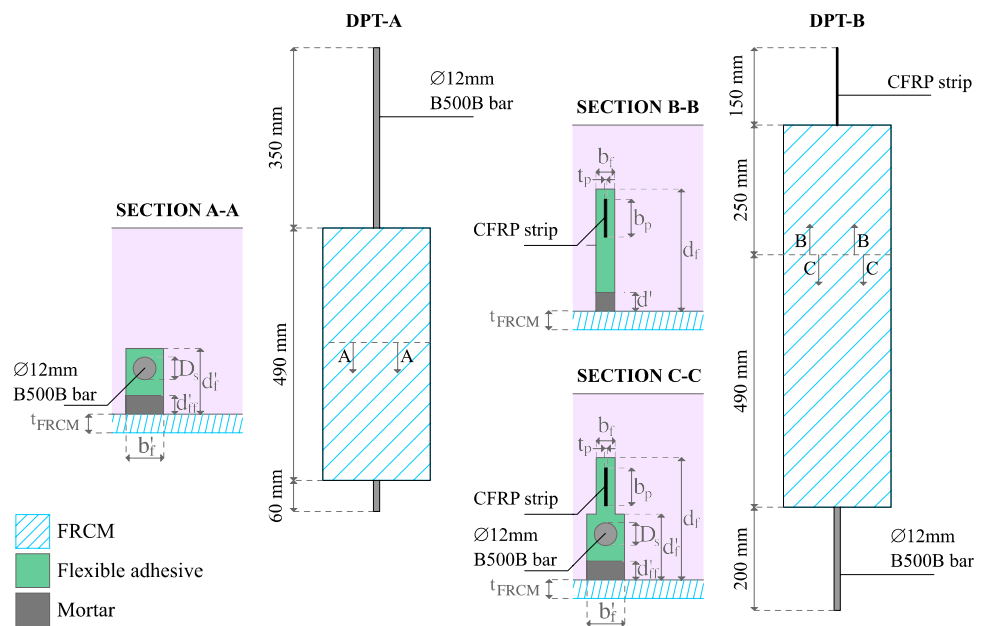


Fig. 10 Overview direct pull-out test setup

rocking of the complete specimen–foundation assembly during pull cycles. This partial detachment of the foundation beam was not observed at the East side during any of the push cycles, leading to different force–displacement behavior in push and pull cycles. It was found that the bracket at the West side of the specimen, which should keep the foundation beam in place was not tightened sufficiently. For specimen M1, uplifting of the foundation beam was observed during the pull cycles. After observing this malfunction, the brackets were tightened further. This detachment of the

foundation beam was not observed during any of the push cycles. During subsequent cycles of the L-specimens, both rocking and sliding of the specimen was observed. Subsequently detachment of the bottom corners next to the steel anchors occurred.

3.3 Strength and drift

The hysteresis loops and backbone curves of all the specimens are provided in Fig. 13, with grey and black colored lines respectively. For all the specimens, a sudden drop in force was observed after the displacement target was reached. This sudden drop was likely a limitation in the hydraulic equipment preventing a smooth transition when the cylinder had to be moved to the opposite direction. The test on specimen S1 was aborted due to the detachment of the foundation beam at a target displacement of 28 mm. The tests on specimens L2 and L3 were stopped due to significant damage development in the region surrounding the anchors. The test on the specimens S2, S3, M1, M2, M3 and L1 were stopped at a target displacement of 40 mm as the maximum stroke of the actuator was reached.

The difference in strength between the West and East side of the specimens, was less than 16% (West side with respect to East side) for all tested walls, except for S2, where the difference was over 50%. From the hysteresis loop of S2 it can be concluded that the East anchor was activated during the push cycles. This was accompanied by a significant increase in the walls capacity in the push direction. Minimal to none activation of the anchorage occurred during the pull cycles. This is expressed in the lower capacity of the wall in the pull direction. After maximum activation of the anchor in

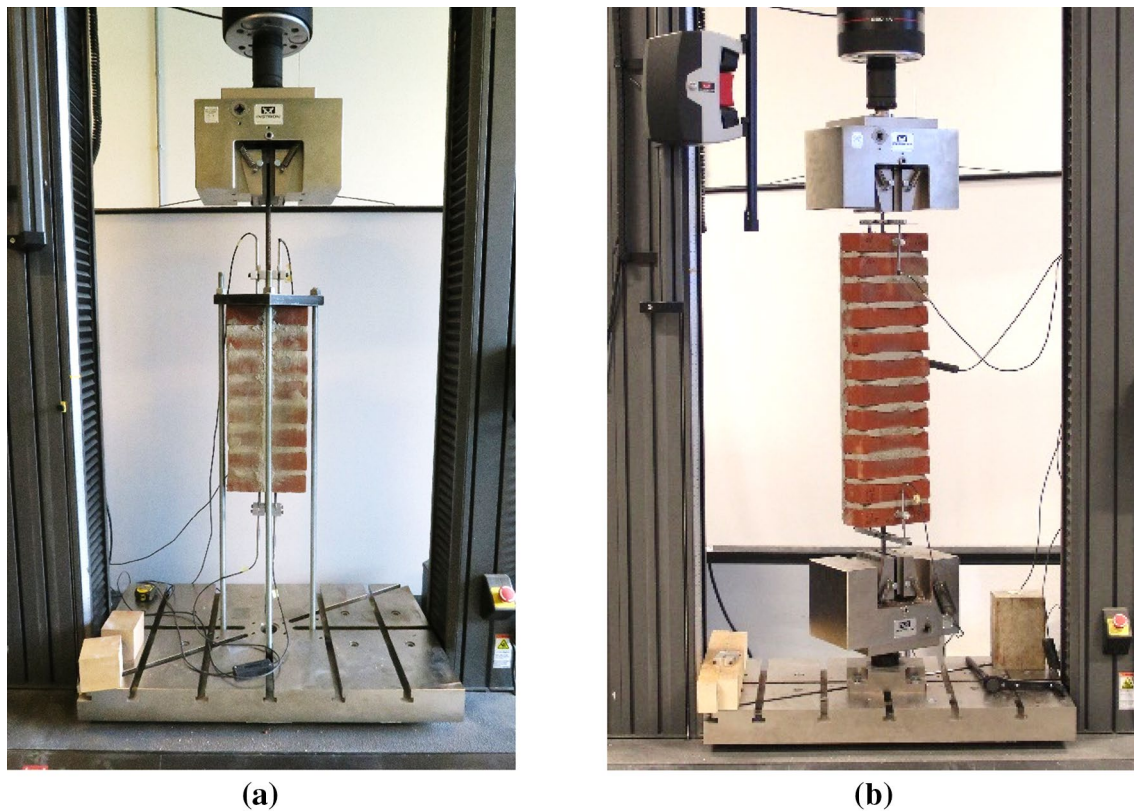


Fig. 11 Direct pull-out test setup for scenario A (a) and scenario B (b)

Table 5 Principal results of the cyclic in-plane shear tests

	L (mm)	q_v (N/mm ²)	$H_{\max,west}$ (kN)	$H_{\max,east}$ (kN)	δ_{\max} (mm)	Δ_{\max} (%)	Failure mode
S1	1100	0.20	13.7	11.9	± 28.6	± 1.17	Rocking
S2	1100	0.30	10.8	22.3	± 40.0	± 1.63	Rocking
S3	1100	0.50	20.4	22.3	± 40.0	± 1.63	Rocking/crushing
M1	2000	0.15	29.4	32.0	± 40.0	± 1.63	Rocking/crushing
M2	2000	0.30	41.0	41.9	± 40.0	± 1.63	Rocking/crushing
M3	2000	0.50	52.6	62.6	± 40.0	± 1.63	Rocking/crushing
L1	4000	0.15	88.5	94.3	± 40.0	± 1.63	Rocking/sliding
L2	4000	0.30	129.1	141.6	± 28.6	± 1.17	Rocking/sliding
L3	4000	0.50	174.5	174.4	± 28.6	± 1.17	Rocking/sliding

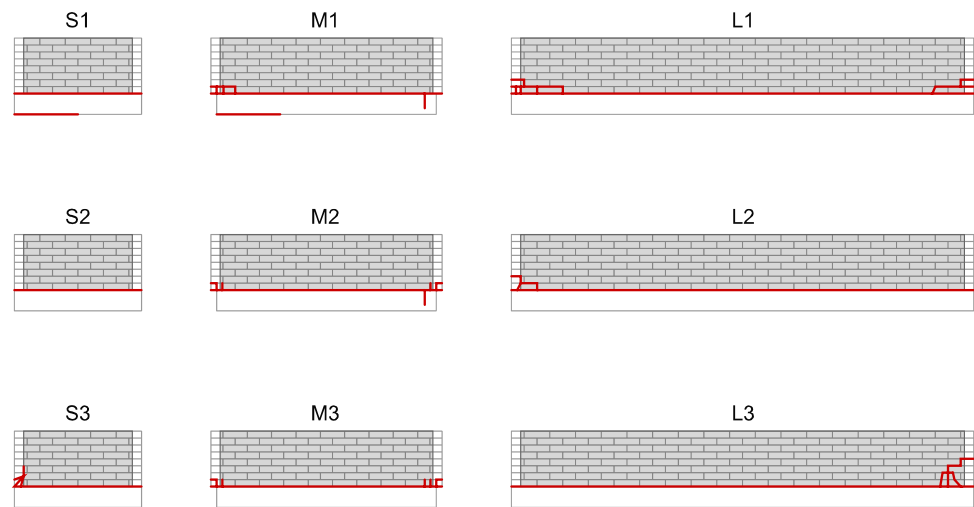
push direction, the force in the load-uplift plot drops back to almost the same value as for the pull cycle. Faulty installation of the anchor could be a possible explanation why the West anchor was minimal to none activated for S2, and thus led to a difference of more than 50% in strength between both sides. The east anchors of both specimen M1 and M2 were pulled out from the foundation, leading to crack formation around the initial location of the anchors in the foundation beam.

Specimens S2 and M1 showed significant different load-displacement behavior between the East and West sides. Looking at the hysteresis loop of specimen S2 on the pull

direction, no drop in force was monitored during the post-peak phase. This shows that the debonding process of the installed anchors was not initiated. As mentioned before, the asymmetry in the load-displacement diagram of specimen M2 was caused by the detachment of the foundation beam during the pull cycles. The West anchor did not reach full strength until a target displacement of 28 mm (versus 6.1 mm for the East anchor).

The axial load has a significant influence on the in-plane resistance of the specimens. For the M and L specimens, a linear correlation was found between the applied axial load and strength of the specimen, with R^2 values of 0.93

Fig. 12 Failure patterns of the S, M and L specimens on the as-built side



and 0.97 respectively. The maximum measured bed joint sliding for the S, M and L specimens were < 1 mm, < 2 mm and > 30 mm respectively.

3.4 Wall response parameters

In-plane wall response parameters were calculated from the force–displacement graphs presented in Fig. 13. A summary of the parameters calculated is shown in Fig. 14.

The bilinearised ultimate wall force H_u is determined in accordance with Eq. (3):

$$H_u = 0.9 H_{\max} \quad (3)$$

The bilinearised initial stiffness K_e is determined in accordance with Eq. (4):

$$K_e = H_u / \delta_e \quad (4)$$

The wall's structural ductility factor μ is the ratio of the ultimate displacement of the wall over the bilinearised yield displacement following Eq. (5):

$$\mu = \delta_u / \delta_e \quad (5)$$

where δ_e is the bilinearised yield displacement and δ_u is the wall's ultimate displacement corresponding to a 20% force drop in the post-peak phase. The wall's response parameters for the tested specimens are listed in Table 6.

The limited stroke of the horizontally oriented hydraulic actuator was insufficient to reach a 20% force drop in the post-peak phase for the specimens S1, S3, L2 and L3. For these specimens, the presented ductility factors in Table 6 are a lower boundary. For the push side of specimen S2, the wall's structural ductility factor was found to be 4.9. For the M specimens, the wall structural ductility factors were in the range of 3.7–14.7. It can be observed that higher axial loads have a positive effect on the mean ductility factor for the M specimens. For specimen L1, the mean ductility factor was

found to be 4.2. Similar to the M specimens, increasing the axial load seems to increase the wall structural ductility factor. An increasing trend in bilinearised initial stiffness was observed as the axial load was increased, while keeping the geometry of the specimen constant.

3.5 Uplift anchors

The uplift of the walls at the moment of the maximum load is provided in Table 7. As the anchorage method was consistent for all specimens, the slip of the anchor (opening between foundation beam and reinforced wall) at maximum applied load was also expected to be consistent. This was not the case as a significant variation was found in the measured uplift values at the failure loads. The observed detachment of the foundation beam was a disturbing factor for the measured uplift of the West anchors of both specimen S1 and M1. The same applies for the West anchor of specimen S2 that did not enter the post-peak phase. The remaining variations in the uplift values, can be explained by the imperfect clamping of the foundation beam, the insufficient tightening of the steel transport plate to the bottom frame and/or the deformation of the used bolt and threaded rods, leading to an uplift of the foundation beam.

3.6 Overview pull-out test results

The results of the direct pull-out tests conducted on masonry prisms with imbedded anchors are shown in Fig. 15, where the pull-out load (pre-tension force not taken into account) is plotted against the loaded end slip of the anchors. The predominant failure mechanism was adhesive failure at the anchor-adhesive interface for both scenarios.

The anchorage strength F_{\max} , mean bond strength σ_{\max} and loaded end slip s_{\max} at maximum pull-out load were

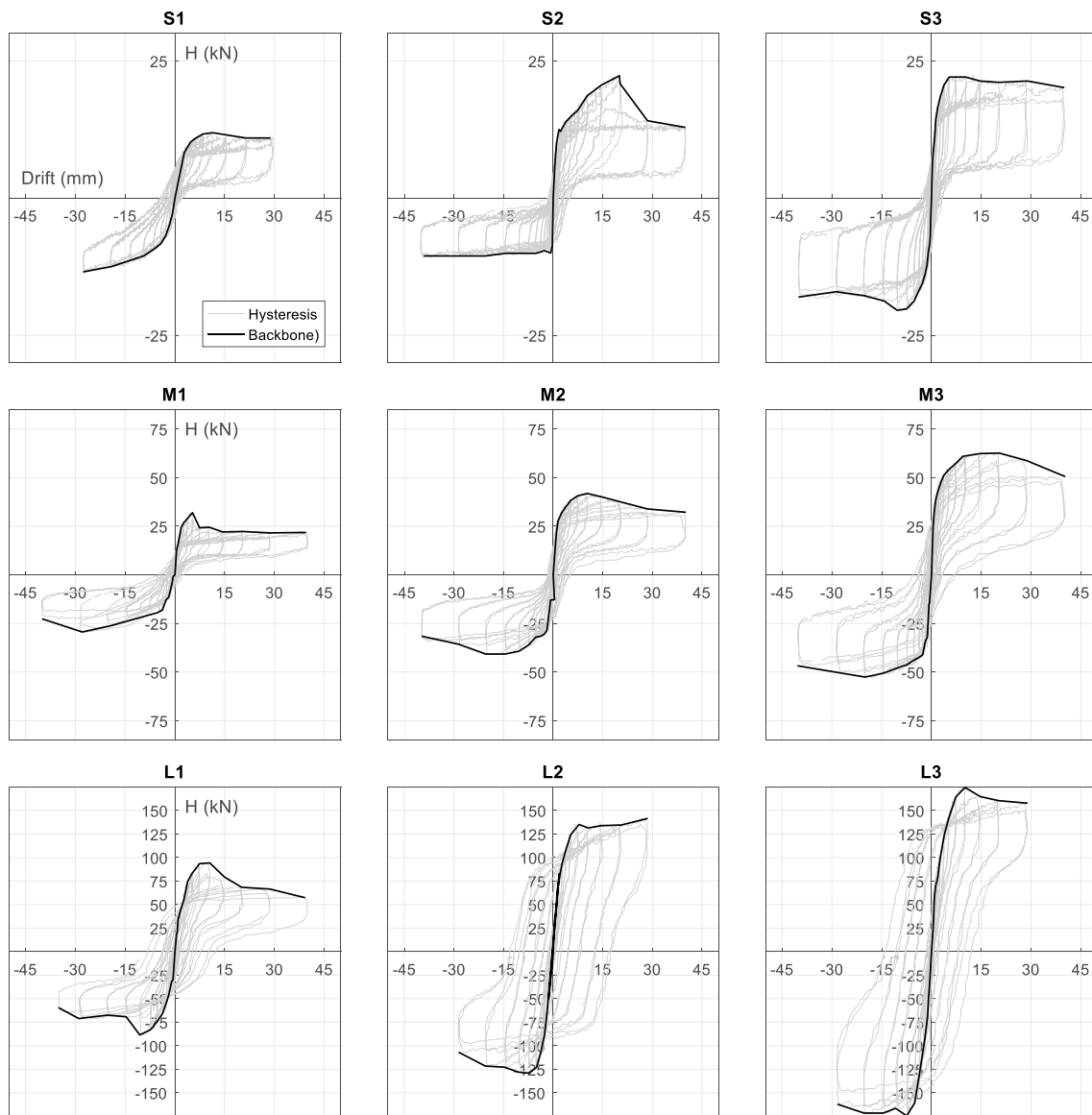


Fig. 13 Hysteresis loops and backbone curves for the S, M and L specimens

determined at 48.78 kN, 2.59 N/mm² and 5.53 mm respectively for the DPT-A-1 and DPT-A-3 specimens. For the DPT-B specimens, these values were found to be 17.90 kN, 0.95 N/mm² and 3.1 mm respectively. The significant lower value in strength for the DPT-B specimens was likely caused by the relatively higher shear stresses in the adhesive mass between the CFRP strip and the anchor, compared to scenario A. These increased shear stresses could have expedited the crack initiation process. The mean initial stiffness $k_{50\%}$, determined at 50% of the strength and the corresponding slip, was found to be 12.30 kN/mm (DPT-A) and 12.78 kN/

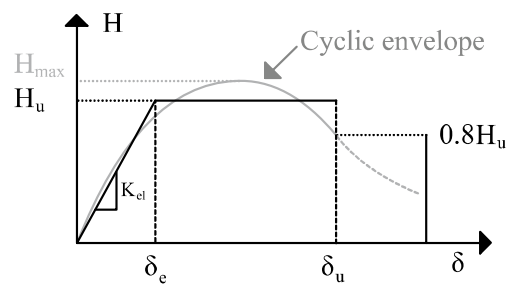


Fig. 14 Equivalent bilinear in-plane wall response parameters Adapted from Magenes and Calvi [40]

Table 6 In-plane wall response parameters for all specimens

		H_{\max} (kN)	H_u (kN)	δ_e (mm)	δ_u (mm)	K_e (kN/mm)	μ [-]
S1	West	11.9	10.7	4.2	> 28.6	2.6	> 6.9
	East	-13.7	-12.3	-8.3	< -28.6	1.5	> 3.5
S2	West	22.3	20.1	8.2	23.2	2.4	4.9
	East	-10.8	-9.7	-0.2	< -40.0	41.8	> 25.0
S3	West	22.3	20.1	1.9	> 40.0	10.7	> 21.3
	East	-20.4	-18.4	-2.6	< -40.0	7.0	> 15.2
M1	West	32.0	28.8	1.9	7.1	15.5	3.7
	East	-29.4	-26.4	-10.7	-38.4	2.5	3.6
M2	West	41.9	37.7	2.4	31.3	15.5	13.0
	East	-41.0	-36.9	-4.3	-36.9	8.5	8.6
M3	West	62.6	56.4	2.7	40.0	20.7	14.7
	East	-52.6	-47.3	-4.2	-40.0	11.4	9.5
L1	West	94.3	84.8	3.6	16.7	23.4	4.6
	East	-88.5	-79.7	-3.8	-14.3	20.8	3.8
L2	West	141.6	127.4	3.6	> 28.6	35.8	> 8.0
	East	-129.1	-116.2	-3.1	< -28.6	37.0	> 9.2
L3	West	174.4	157.0	4.4	> 28.6	36.0	> 6.6
	East	-174.5	-157.1	-3.7	< -28.6	42.9	> 7.8

mm (DPT-B). For the DPT-A-1 and DPT-A-3 specimens, a reduction in stiffness was observed at a loaded end slip of approximately 4 mm (s_{damage}). For specimen DPT-A-2, the damage initiation stage was entered earlier due to incorrect surface preparation (not made dust free and not made clean with acetone), and thus leading to a significant lower anchorage strength. For the DPT-B specimens, a reduction in stiffness was observed at a significant lower slip (1 mm). An overview of the obtained direct pull-out test results are provided in Table 8.

Looking at values for the corresponding slip at full strength, a major difference was found with the values presented in Table 6. This indicates that the aforementioned disturbing factors in the measurement of the uplift of the anchors, could have an even more significant contribution than previously assumed.

4 Analytical model based on Eurocode 6

When out-of-plane buckling is not considered, then there are two failure modes that can occur for walls loaded in-plane: moment failure/rocking or shear failure. The governing

failure mode is influenced by the aspect ratio (height divided by length) and the ratio between the vertical and horizontal loading. The moment and shear resistance of reinforced walls were modelled using modified rules from Eurocode 6 [42]. The behavior and resistance of a reinforced wall is very much alike that of an unreinforced wall. This with the exception that a tension element (anchor) in vertical direction is present. Therefore some modifications on the existing equations for unreinforced masonry walls were made. The used mechanical model is presented in Fig. 16.

4.1 Moment failure

The ultimate eccentricity e_u is determined using Eq. (6). The ultimate depth of the compression zone x_u , following Eq. (7), is based on a bi-linear stress-strain relation for the masonry (Fig. 15) according to the Dutch NA [41] to Eurocode 6 [42].

$$e_u = \frac{l_w}{2} - \frac{67}{189}x_u \quad (6)$$

$$x_u = \frac{14}{9} \frac{(F_v + F_{v,r})}{t_w \cdot f_m} \quad (7)$$

Table 7 The uplift of the anchor at maximum applied force

	Unit	S1	S2	S3	M1	M2	M3	L1	L2	L3
Uplift east anchor	mm	3.10	4.49	3.48	2.47	6.24	11.12	7.81	12.76	7.86
Uplift west anchor	mm	8.88	14.31	2.14	18.68	13.42	12.07	9.50	3.88	4.50

where f_m is the compressive strength of the masonry, $F_{v,r}$ is the tensile force in the anchors and F_v is the axial force following Eq. (8). The own weight of the reinforced wall ($\gamma = 2.12 \text{ kN/m}^2$) is also taken into account for the determination of the axial force.

$$F_v = q_v l_w + (l_w \cdot h_w) \gamma \tag{8}$$

The moment resistance M_R follows from Eq. (9). The resistance is based on the equilibrium of the wall, which is influenced by the ultimate eccentricity e_u of the vertical reaction force F_v and the tensile force in the anchors $F_{v,r}$

$$M_R = (F_v + F_{v,r}) e_u + F_{v,r} \left(d - \frac{l_w}{2} \right) \tag{9}$$

The effective depth d of the anchors is determined in accordance with Eq. (10)

$$d = l_w - l_{edge} \tag{10}$$

Combing Eqs. (6–10) results in Eq. (11):

$$M_R = (F_v + F_{v,r}) \left\{ \frac{l_w}{2} - \frac{67}{189} \frac{14}{9} \frac{(F_v + F_{v,r})}{t_w \cdot f_m} \right\} + F_{v,r} \left(\frac{l_w}{2} - l_{edge} \right) \tag{11}$$

The moment resistance M_R that follows from the experiments is determined by Eq. (12):

$$M_R = F_{h,test} \cdot h_w \tag{12}$$

Combing and rewriting Eqs. (11) and (12), results in Eq. (13), which can be used to determine the tensile forces in the anchors according to the proposed model. The α and β factors in Eq. (13) are determined using Eqs. (14) and (15) respectively.

$$F_{v,r} = \frac{\beta + l_w - (2\alpha F_v + l_{edge})}{2\alpha} \tag{13}$$

$$\alpha = \frac{67}{189} \frac{14}{9} \frac{1}{t_w \cdot f_m} \tag{14}$$

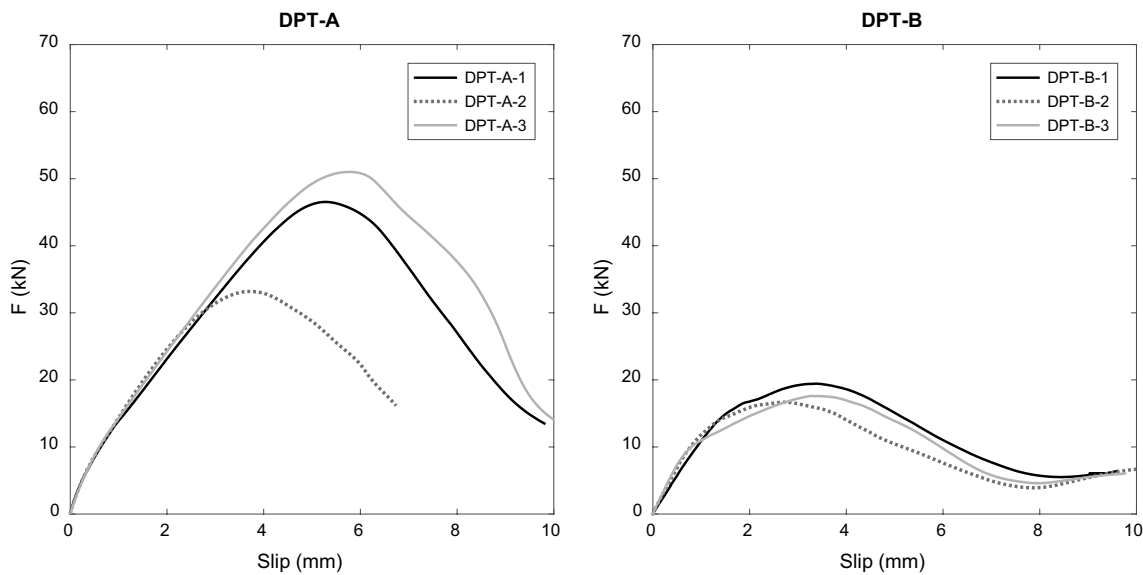


Fig. 15 Force-slip (free end) diagrams of the direct-pull-out tests

Table 8 Overview pull-out test results

	F_{max} (kN)	σ_{max} (N/mm ²)	s_{max} (mm)	$k_{50\%}$ (kN/mm)	s_{damage} (mm)
DPT-A-1	46.54	2.47	5.28	11.55	± 4.0
DPT-A-2	33.18 ^a	1.76 ^a	3.71 ^a	13.38	± 2.5
DPT-A-3	51.01	2.71	5.78	11.97	± 4.0
Mean	48.78	2.59	5.53	12.30	
DPT-B-1	19.43	1.03	3.36	11.05	± 1.5
DPT-B-2	16.67	0.88	2.68	13.59	± 1.0
DPT-B-3	17.60	0.93	3.27	13.70	± 1.0
Mean	17.90	0.95	3.10	12.78	

^aNot included in the mean calculation

Table 10 Overview results analytical model for specimens (S and M) failing due to rocking

	F_v (kN)	F_{Rh} (kN)	$V_{R,s0}$ (kN)	$F_{h,test}$ (kN)	$F_{Rh}/F_{h,test}$ (-)	$F_{v,r}$ (kN)
Eqs.		(16)	(20)			(13)
S1	27.7	6.1	20.8	13.7	0.45	20.2
S2	38.7	8.5	29.0	22.3	0.38	37.3
S3	60.7	13.1	45.5	22.3	0.59	25.2
M1	40.4	15.7	30.3	32.0	0.51	21.3
M2	70.4	27.1	52.8	41.9	0.67	19.0
M3	110.4	41.9	82.8	62.6	0.69	27.0

can be concluded that the effect of anchors for increasing the rocking capacity is significant for the *S* and *M* specimens, with model/experimental ($F_{Rh}/F_{h,test}$) ratios in the range of 0.38–0.59 and 0.51–0.69 for the *S* and *M* specimens respectively. Looking at Fig. 17, it is observed that the rocking capacity of specimen *S2* was not influenced by the West anchor. Combined with the previously mentioned absence of the post-peak phase of the anchor bond, the conducted analyses indicate that the West anchor of specimen *S2* was not activated during the experiment. Faulty surface conditions of the anchor (not cleaned and made dust-free) could not be the only explanation, as the direct pull-out results indicated that there still was some significant bonding capacity left in this case. Possible explanations for the West anchor not being activated could be the insufficient confinement of the anchor in the flexible adhesive and/or the faulty preparation of the flexible adhesive.

For the specimens where sliding over the base joint occurred (*L* specimens), the ratio between the maximum horizontal force on the specimen and the calculated shear sliding resistance ($V_{Rs}/F_{h,test}$) is < 1.0 , as shown in Table 11. For the *L*-specimens, the dark grey areas in Fig. 17 indicate the difference between the maximum load during the in-plane experiments and the sliding resistance V_{Rs} of the specimen including the extra compression force caused by the anchor (indicated by a dash-dot line). Comparing the determined values for the sliding resistance with and without the contribution of the anchors from Table 11, it can be observed that the additional compression force due to the anchors results in an increase of 14.8 kN (+24.5%) and 15.2 (+14.42%) in sliding shear resistance (following the analytical model) for specimens *L1* and *L2* respectively. For specimen *L3* the sliding shear resistance for the two aforementioned cases remained the same. It should be noted that dowel action of the anchor in the compressed area was not considered for the values regarding the resistance of the base joint. The contribution of the anchors in creating an additional compression force in the joint will result in an extra resistance against sliding due to friction, hence probably explaining the specimen exceeding the calculated sliding resistance V_{Rs} . Looking at the values for the rocking

resistance F_{Rh} in case of no anchors and the resistance V_{Rs} against shear sliding in the base joint for specimens *L1* and *L2* (as provided in Table 11), it can be observed that the anchors first provide additional sliding resistance followed by an increased moment resistance, preventing the rocking failure of the specimen. The added value of the anchors is limited for both the rocking and sliding behavior of specimen *L3*, likely caused by the high axial load.

For the *S* and *M* specimens the determined tensile forces in the anchors using Eq. (13) ranged between 11.7 and 37.3 kN, with a mean value of 20.1 kN (COV = 38.7%). Comparing the values for the analytically determined anchorage strength from the in-plane experiments with the conducted direct pull-out experiments, the calculated values predominantly fall between the lower bound (scenario B) and the upper bound (scenario A) as shown in Fig. 18. It can be concluded that scenario B, where the tensile forces are pre-dominantly transferred from the anchor to CFRP strip, provided a better approximation of the analytically determined anchorage strength. Testing conform scenario A is not advised in the current study, as the anchorage strength is significantly overestimated.

Taking 17.9 kN as the mean strength of the anchors (following the pull-out tests conform scenario B), the (moment) resistance of the wall F_R can be determined for the *S* and *M* specimens. The results are shown in Table 12 and Fig. 19. The model/experimental ratio was in the range 0.68–1.08 and 0.90–1.07 for the *S* and *M* specimens respectively. The model/experimental ratio of 1.4 for specimen *S2* (east) was not included in Fig. 19 as the West anchor minimally to not activated, as was shown in Fig. 17.

With the mean strength of the anchors (following the pull-out tests conform scenario B), the (sliding) resistance of the wall F_R can also be determined for the *L* specimens. The results are provided in Table 13 and Fig. 19. The model/experimental ratio was in the range 0.78–1.03 for the *L* specimens. The low ratios can partly be explained by the dowel effect of the anchor in the compression zone not being taken into account.

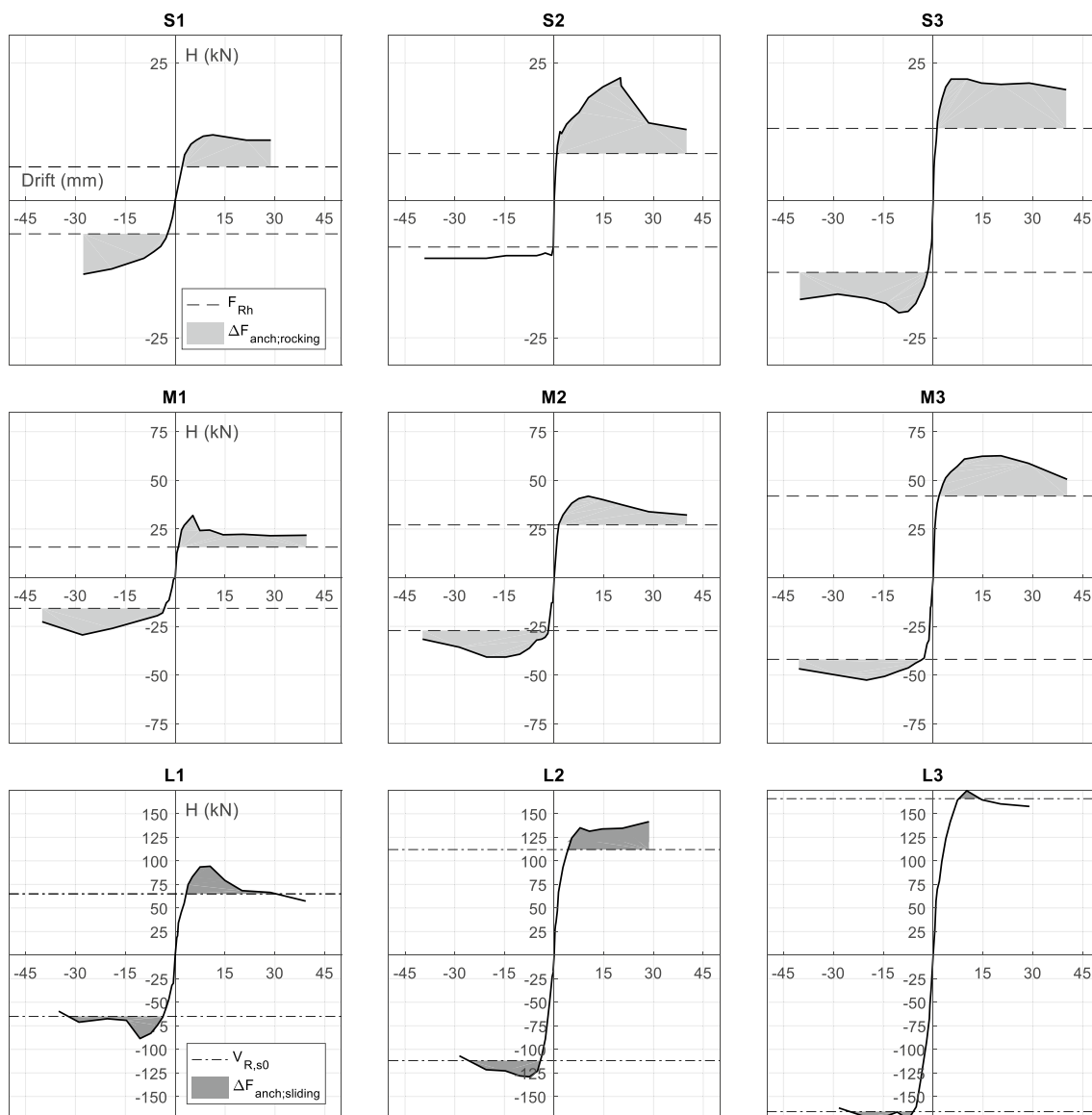


Fig. 17 Marked backbone curves for the S, M and L specimens, with the added value of the anchors for the rocking capacity (light grey areas), and for the sliding resistance (dark grey areas)

5 Conclusions

An experimental study was presented that consisted of nine masonry walls retrofitted with a single-sided Fabric-Reinforced Cementitious Matrix (FRCM) layer, DM CFRP strips and flexible anchor connection. Three different wall geometries, with three different axial loads per geometry were tested to investigate the cyclic in-plane behavior of the reinforced masonry walls. Additional pull-out experiments considering two stress distribution scenarios (tensile force in anchor transferred to (A) masonry or (B) CFRP strip) were performed on prisms with steel anchors to determine the

anchoring strength in the flexible adhesive. The following can be concluded from the study:

- None of the specimens showed any shear damage at both the reinforced and as-built surfaces during the cyclic in-plane experiments. Cracking and eventually sliding always occurred at the interface between the bottommost bed-joint and the concrete foundation beam.
- The S specimen loaded by a high axial load and all M specimens had rocking and toe-crushing as pre-dominant failure mechanism. The S specimens with low and moderate axial loads only showed rocking behaviour. The

Table 11 Overview results analytical model for specimens (L) failing due to sliding

	F_v (kN)	F_{Rh} (kN)	$V_{R,s0}$ (kN)	$F_{h,test}$ (kN)	$V_{R,s0}/F_{h,test}$ (-)	$F_{v,r}$ (kN)	$V_{R,s}$ (kN)	$V_{R,s}/F_{h,test}$ (-)
Eqs.		(16)	(20)			(13)	(19)	
L1	80.8	65.0	60.6	94.3	0.64	19.8	75.4	0.80
L2	140.8	111.9	105.6	141.6	0.75	20.3	120.8	0.85
L3	220.8	172.9	165.6	174.5	0.95	1.1	166.4	0.95

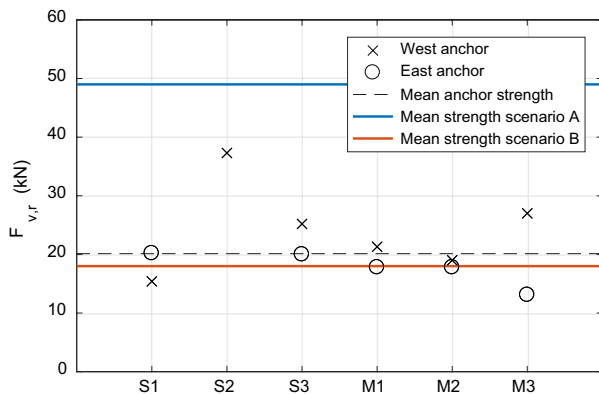


Fig. 18 Comparison calculated and tested anchor strength

large specimens showed a combined flexure and sliding failure mode.

- For the M specimens the wall’s structural ductility factors were in the range of 3.7–14.7. For specimen L1, the mean ductility factor was found to be 4.2. For the remaining specimens a lower bound (in the range 3.5–25.0) was determined as the limited stroke of the horizontally oriented hydraulic actuator was insufficient to reach a 20% force drop in the post-peak phase. The exact value could not be determined do to the limitations of the in-plane shear test setup.
- The mean anchor strength as determined with the direct pull-out experiments for scenario A, where the tensile forces in the anchor were transferred to the masonry, was

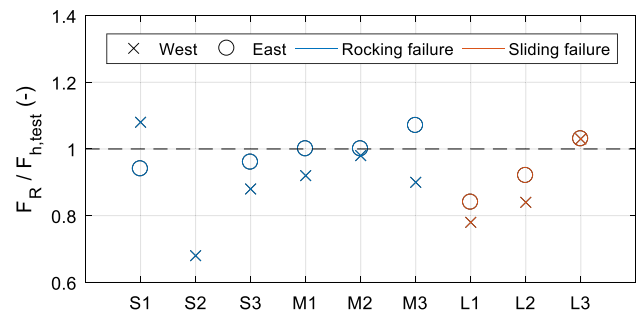


Fig. 19 Model/experimental ratios for all specimens

found to be 49 kN. For scenario B, where the tensile forces in the anchor were transferred to CFRP strip (due to the chosen boundary conditions), the mean anchor strength was considerably lower at 18 kN. This was likely due to the relatively higher shear deformations of the adhesive between the CFRP strip and the anchor (scenario B) when compared to the shear deformations of the adhesive between the CFRP strip and the masonry (scenario A).

- For the mean initial stiffness $k_{50\%}$ of the anchorage (from origin until 50% of the strength) no significant differences were found between the results obtained by direct pull-out testing with scenario A (12.3 kN/mm) and scenario B (12.8 kN/mm).

Table 12 Comparison analytical model ($F_{v,r} = 17.9$ kN) and experimental results for the specimens (S and M) failing predominantly due to rocking

	$F_{h,test, east}$ (kN)	$F_{h,test, west}$ (kN)	F_{Rh} (kN)	V_{Rs} (kN)	$F_R = \min(F_{Rh}, V_{Rs})$ (kN)	$F_{RM}/F_{h,test, east}$ (-)	$F_{RM}/F_{h,test, west}$ (-)
Eqs.			(16)	(20)			
S1	13.7	11.9	12.8	47.6	12.8	0.94	1.08
S2	10.8	22.3	15.2	55.9	15.2	1.40 ^a	0.68
S3	20.4	22.3	19.6	72.4	19.6	0.96	0.88
M1	29.4	32	29.5	57.1	29.5	1.00	0.92
M2	41	41.9	41.1	79.6	41.1	1.00	0.98
M3	52.6	62.6	56.1	109.6	56.1	1.07	0.90

^aAnchor not activated

Table 13 Comparison analytical model ($F_{v,r} = 17.9 \text{ kN}$) and experimental results for the specimens (L) failing predominantly due to sliding

	$F_{h,\text{test,east}}$ (kN)	$F_{h,\text{test,west}}$ (kN)	F_{R_h} (kN)	V_{R_s} (kN)	$F_R = \min(F_{R_h}; V_{R_s})$ (kN)	$F_R/F_{h,\text{test,east}}$ (-)	$F_R/F_{h,\text{test,west}}$ (-)
Eqs.			(16)	(20)			
L1	88.5	94.3	91.5	87.4	87.4	0.84	0.78
L2	129.1	141.6	138.2	132.4	132.4	0.92	0.84
L3	174.5	174.4	198.7	192.4	192.4	1.03	1.03

- A mechanical model based on EC6 was proposed to model the capacity of the reinforced walls during in-plane loading, covering both moment failure and shear sliding failure. The mechanical model provided a good approximation of the experimentally obtained ultimate loads, with model/experimental ratios in the range of 0.68–1.08 and 0.78–1.03 for the specimens predominantly failing due to rocking (S and M specimens) and sliding (L specimens) respectively. The sliding resistance following the model was conservative because the dowel effect of the anchor in the compression zone was not taken into account.
- Due to the application of the anchors and the single-sided FRCM overlay, the analytical model provides moment resistance amplification factors (moment resistance reinforced masonry/moment resistance URM) in the ranges 1.5–2.1, 1.3–1.8 for the S and M specimens respectively.
- Using the analytical model and the in-plane test results of the S and M specimens the determined tensile forces in the anchors ranged between 19.0 kN and 37.3 kN, with a mean value of 20.1 kN (COV = 38.7%). The results obtained from the direct pull-out experiments conform scenario B (mean anchorage strength 17.9 kN) provided a good approximation of the analytically determined anchorage strength. The anchorage strength is significantly overestimated when the pull-out experiments are conducted conform scenario A.

Acknowledgements The authors wish to gratefully acknowledge the support by QuakeShield, a joint venture between Royal Oosterhof Holman and SealteQ Group. The technical assistance and guidance received from the staff of the Structural Design Unit at Eindhoven University of Technology is also gratefully acknowledged. Special thanks to our beloved and retiring colleague Dr. Ir. A.T. Vermeltoort, who provided insight and expertise that greatly assisted the research. Wishing you a long and joyous retirement.

Open Access This article is distributed under the terms of the Creative Commons Attribution 4.0 International License (<http://creativecommons.org/licenses/by/4.0/>), which permits unrestricted use, distribution, and reproduction in any medium, provided you give appropriate credit to the original author(s) and the source, provide a link to the Creative Commons license, and indicate if changes were made.

References

1. Bourne S, Oates S (2017) Development of statistical geomechanical models for forecasting seismicity induced by gas production from the Groningen field. *Neth J Geosci* 96(5):S175–S182. <https://doi.org/10.1017/njg.2017.35>
2. Van Thienen-Visser K, Breunese JN (2015) Induced seismicity of the Groningen gas field: history and recent developments. *Lead Edge* 34(6):664–671. <https://doi.org/10.1190/tle34060664.1>
3. Türkmen ÖS, De Vries BT, Wijte SNM, Vermeltoort (2019) In-plane behavior of clay brick masonry wallettes retrofitted with single-sided fabric-reinforced cementitious matrix and deep mounted carbon fibre strips. *Bull Earthq Eng* (in press)
4. Triantafillou TC (1998) Strengthening of masonry structures using epoxy-bonded FRP laminates. *J Compos Constr* 2(2):96–104
5. Papanicolaou CG, Triantafillou TC, Papathanasiou M, Karlos K (2007) Textile reinforced mortar (TRM) versus FRP as strengthening material of URM walls: out-of-plane cyclic loading. *Mater Struct* 41(1):143–157. <https://doi.org/10.1617/s11527-007-9226-0>
6. Maalej M, Lin V, Nguyen M, Quek S (2010) Engineered cementitious composites for effective strengthening of unreinforced masonry walls. *Eng Struct* 32(8):2432–2439. <https://doi.org/10.1016/j.engstruct.2010.04.017>
7. Parisi F, Iovinella I, Balsamo A, Augenti N, Prota A (2013) In-plane behaviour of tuff masonry strengthened with inorganic matrix-grid composites. *Compos B Eng* 45(1):1657–1666. <https://doi.org/10.1016/j.compositesb.2012.09.068>
8. Bilotta A, Ceroni F, Nigro E, Pecce M (2017) Experimental tests on FRCM strengthening systems for tuff masonry elements. *Constr Build Mater* 138:114–133. <https://doi.org/10.1016/j.conbuildmat.2017.01.124>
9. Nanni A (2012) A new tool for concrete and masonry repair. *Concr Int* 34(4):1–7
10. Papanicolaou CG, Triantafillou TC, Papathanasiou M, Karlos K (2008) Textile reinforced mortar (TRM) versus FRP as strengthening material of URM walls: out-of-plane cyclic loading. *Mater Struct* 41(1):143–157. <https://doi.org/10.1617/s11527-007-9226-0>
11. Ascione L, Felice GD, Santis SD (2015) A qualification method for externally bonded fibre reinforced cementitious matrix (FRCM) strengthening systems. *Compos B Eng* 78:497–506. <https://doi.org/10.1016/j.compositesb.2015.03.079>
12. Corinaldesi V, Donnini J, Mazzoni G (2014) Experimental study of adhesion between FRCM and masonry support. *Key Eng Mater* 624:189–196. <https://doi.org/10.4028/www.scientific.net/kem.624.189>
13. Donnini J, Corinaldesi V (2017) Mechanical characterization of different FRCM systems for structural reinforcement. *Constr Build Mater* 145:565–575. <https://doi.org/10.1016/j.conbuildmat.2017.04.051>
14. Babaeidarabad S, De Caso F, Nanni A (2013) URM walls strengthened with mesh-reinforced cementitious matrix composite

- subjected to diagonal compression. *J Compos Constr.* [https://doi.org/10.1061/\(ASCE\)CC.1943-5614.0000441](https://doi.org/10.1061/(ASCE)CC.1943-5614.0000441)
15. Ismail N (2012) Selected strengthening techniques for the seismic retrofit of unreinforced masonry buildings (doctoral dissertation). <https://researchspace.auckland.ac.nz/bitstream/handle/2292/19106/whole.pdf?sequence=2>. Accessed 2 Oct 2018
 16. Shabdin M, Zargar M, Attari NK (2018) Experimental diagonal tension (shear) test of un-reinforced masonry (URM) walls strengthened with textile reinforced mortar (TRM). *Constr Build Mater* 164:704–715. <https://doi.org/10.1016/j.conbuildmat.2017.12.234>
 17. Marcari G, Basili M, Vestroni F (2017) Experimental investigation of tuff masonry panels reinforced with surface bonded basalt textile-reinforced mortar. *Compos B Eng* 108:131–142. <https://doi.org/10.1016/j.compositesb.2016.09.094>
 18. Faella C, Martinelli E, Nigro E, Paciello S (2010) Shear capacity of masonry walls externally strengthened by a cement-based composite material: an experimental campaign. *Constr Build Mater* 24(1):84–93. <https://doi.org/10.1016/j.conbuildmat.2009.08.019>
 19. Ismail N, Ingham JM (2016) In-plane and out-of-plane testing of unreinforced masonry walls strengthened using polymer textile reinforced mortar. *Eng Struct* 118:167–177. <https://doi.org/10.1016/j.engstruct.2016.03.041>
 20. Augenti N, Parisi F, Prota A, Manfredi G (2011) In-plane lateral response of a full-scale masonry subassembly with and without an inorganic matrix-grid strengthening system. *J Compos Constr* 15(4):578–590. [https://doi.org/10.1061/\(asce\)cc.1943-5614.0000193](https://doi.org/10.1061/(asce)cc.1943-5614.0000193)
 21. Prota A, Marcari G, Fabbrocino G, Manfredi G, Aldea C (2006) Experimental in-plane behavior of tuff masonry strengthened with cementitious matrix-grid composites. *J Compos Constr* 10(3):223–233. [https://doi.org/10.1061/\(asce\)1090-0268\(2006\)10:3\(223\)](https://doi.org/10.1061/(asce)1090-0268(2006)10:3(223))
 22. Sagar SL, Singhal V, Rai DC, Gudur P (2017) Diagonal shear and out-of-plane flexural strength of fabric-reinforced cementitious matrix-strengthened masonry wallets. *J Compos Constr* 21(4):04017016. [https://doi.org/10.1061/\(asce\)cc.1943-5614.0000796](https://doi.org/10.1061/(asce)cc.1943-5614.0000796)
 23. Türkmen ÖS, Vermeltoort AT, Martens DRW (2016) Seismic retrofit system for single leaf masonry buildings in Groningen. In: Proceedings of 16th International brick and block masonry conference, 26–30 June 2016, Padova, Italy, pp 1–8
 24. Türkmen ÖS, Wijte SNM, Vermeltoort AT, Martens DRW (2017) Experiments to determine the out-of-plane behavior of CFRP and ductile adhesive reinforced clay brick masonry walls. In: Proceedings 13th Canadian masonry symposium
 25. Dizhur D, Griffith MC, Ingham JM (2014) Pullout strength of NSM CFRP strips bonded to vintage clay brick masonry. *Eng Struct* 69:25–36. <https://doi.org/10.1016/j.engstruct.2014.02.006>
 26. Türkmen ÖS, Wijte SNM, Ingham JM, Vermeltoort AT (2018) Bond slip behaviour of deep mounted carbon fibre reinforced polymer strips confined with a ductile adhesive in clay brick masonry. In: Masia M, Alternam D, Totoev Y, Page A (eds), Proceedings of 10th Australasian masonry conference: masonry today and tomorrow, blz. 672–686
 27. Kwiecień A (2012) Stiff and flexible adhesives bonding CFRP to masonry substrates—investigated in pull-off test and Single-Lap test. *Arch Civil Mech Eng* 12(2):228–239. <https://doi.org/10.1016/j.acme.2012.03.015>
 28. Derkowski W, Kwiecień A, Zajac B (2013) CFRP strengthening of bent RC elements using stiff and flexible adhesives. *Tech Trans* 1-B/2013:37–52
 29. European Committee for Standardization (2015) EN 772-1:2011 + A1:2015: methods of test for masonry units—Part 1: determination of compressive strength. European Committee for Standardization, Brussels
 30. ASTM (2007) C1006-07: standard test method for splitting tensile strength of masonry units, 2007. ASTM International, West Conshohocken
 31. ASTM (2003) ASTM C67-03a, standard test methods for sampling and testing brick and structural clay tile. ASTM International, West Conshohocken
 32. European Committee for Standardization (2007) EN 1015-11:1999/A1:2007: methods of test for mortar for masonry—part 11: determination of flexural and compressive strength of hardened mortar. European Committee for Standardization, Brussels
 33. European Committee for Standardization (1998) NEN-EN 1052-1:1998: methods of test for masonry—part 1: determination of compressive strength. European Committee for Standardization, Brussels
 34. European Committee for Standardization (2007) EN 1052-3:2002/A1:2007: methods of test for masonry—part 3: determination of initial shear strength. European Committee for Standardization, Brussels
 35. Jafari S, Rots JG, Esposito R, Messali F (2017) Characterizing the material properties of dutch unreinforced masonry. *Procedia Eng* 193:250–257. <https://doi.org/10.1016/j.proeng.2017.06.211>
 36. NEN (2017) NPR 9998:2017: Beoordeling van de constructieve veiligheid van een gebouw bij nieuwbouw, verbouw en afkeuren—Grondslagen voor aardbevingsbelastingen: geïnduceerde aardbevingen. Nederlands Normalisatie-Instituut, Delft
 37. ISO 527-1: 2012. (2018). plastics-determination of tensile properties—part 1: general principles
 38. AC434-13 (2013) Acceptance criteria for masonry and concrete strengthening using fiber reinforced cementitious matrix (FRCM) composite systems. ICC Evaluation Service, Whittier
 39. FEMA (2007) 461/Interim testing protocols for determining the seismic performance characteristics of structural and nonstructural components. Applied Technology Council, Redwood City, p 113
 40. Magenes G, Calvi GM (1997) In-plane seismic response of brick masonry walls. *Earthq Eng Struct Dyn* 26(11):1091–1112
 41. European Committee for Standardization (2006) Eurocode 6: design of masonry structures—part 1-1: general rules for reinforced and unreinforced masonry structures. European Committee for Standardization, Brussels
 42. NEN-EN (2005). 1996-1-1: Design of masonry structures—Part 1-1: General rules for reinforced and unreinforced masonry structures

Publisher's Note Springer Nature remains neutral with regard to jurisdictional claims in published maps and institutional affiliations.